INTERNATIONAL JOURNAL FOR NUMERICAL METHODS IN FLUIDS
Int. J. Numer. Meth. Fluids 2003; **41**:863–879 (DOI: 10.1002/fld.472)

Validations of CFD against detailed velocity and pressure measurements in water turbine runner flow

H. Nilsson*,† and L. Davidson

Chalmers University of Technology, Department of Thermo and Fluid Dynamics, SE-412 96 Göteborg, Sweden

SUMMARY

This work compares CFD results with experimental results of the flow in two different kinds of water turbine runners. The runners studied are the GAMM Francis runner and the Hölleforsen Kaplan runner. The GAMM Francis runner was used as a test case in the 1989 *GAMM Workshop on 3D Computation of Incompressible Internal Flows* where the geometry and detailed best efficiency measurements were made available. In addition to the best efficiency measurements, four off-design operating condition measurements are used for the comparisons in this work. The Hölleforsen Kaplan runner was used at the 1999 *Turbine 99* and 2001 *Turbine 99—II* workshops on draft tube flow, where detailed measurements made after the runner were used as inlet boundary conditions for the draft tube computations. The measurements are used here to validate computations of the flow in the runner.

The computations are made in a single runner blade passage where the inlet boundary conditions are obtained from an extrapolation of detailed measurements (GAMM) or from separate guide vane computations (Hölleforsen). The steady flow in a rotating co-ordinate system is computed. The effects of turbulence are modelled by a low-Reynolds number $k-\omega$ turbulence model, which removes some of the assumptions of the commonly used wall function approach and brings the computations one step further.

The computational results are compared to the measurements with respect to detailed velocity and pressure distributions at several measurement sections and several operating conditions. The computational results are also compared to coarse grid wall function computations by the TASCflow CFD code, which uses a similar methodology as the CALC-PMB CFD code used in the present work. The comparisons show where the computational method is sufficient and where it is not sufficient. The behaviour of the computational method is similar for both kinds of water turbines, which shows that experience of computations in water turbines will ultimately give quantitatively correct results. Copyright © 2003 John Wiley & Sons, Ltd.

KEY WORDS: CFD; low-Reynolds; validation; water turbine

* Correspondence to: H. Nilsson, Department of Thermo and Fluid Dynamics, Chalmers University of Technology, SE-412 96 Göteborg, Sweden.
† E-mail: hani@tfd.chalmers.se

Contract/grant sponsor: ELFORSK (Swedish Electrical Utilities Research and Development Company)
Contract/grant sponsor: Swedish National Energy Administration;
Contract/grant sponsor: GE Energy (Sweden) AB

Received January 2002
Revised 9 November 2002

1. BACKGROUND

The flow in water turbines has been investigated numerically for decades. There are 1D, 2D, quasi-3D and 3D numerical methods [1] that approximate the flow in water turbines with increasing levels of accuracy and detail. All these methods have their own advantages and application areas. 1D, 2D and quasi-3D methods are fast but model some or all of the three-dimensionality of the flow. To study the flow in water turbines in detail a 3D numerical method is needed. The Euler method is an example of a 3D numerical method that is still quite frequently used for computations of water turbine flow [2]. The Euler method neglects the effects of viscosity and turbulence. The results from Euler computations of water turbines at best efficiency operating condition can be quite reliable. However, when it comes to off-design operating conditions the viscous and turbulent effects become more and more important. During the most recent decades the computational methods for turbomachinery have been undergoing a transition from inviscid flow to viscous flow. Some of the recent work on numerical prediction of the flow in water turbines can be found in journal papers [3, 4], but most of it is found in conference proceedings such as the proceedings of the biennial IAHR symposiums on Hydraulic Machinery and Systems [5].

Most work on 3D turbulent water turbine runner flow in the literature compute the steady periodic flow in a single runner blade passage in order to save computational effort. Some work present computations of the complete runner [6] and some work attempt to couple the whole system, from the inlet of the spiral casing to the outlet of the draft tube [7]. Almost all work use wall functions in order to save computational effort and often the results are presented without validation against detailed velocity and pressure measurements. The present work computes the 3D turbulent water turbine runner flow in a single runner blade passage but brings the computations one step further by using a low-Reynolds number turbulence model. The integration up to the wall and a fine resolution of the viscous sublayer cannot be avoided if transition phenomena and accurate wall friction are to be solved [8]. Low-Reynolds number turbulence models resolve the boundary layers and remove some of the assumptions of the wall function approach. It is necessary to use a low-Reynolds number turbulence model approach if the computations include hub and tip clearance flow in Kaplan turbines, and guide vane clearance flow. The method is applied on the flow in two kinds of water turbine runners and the computational results are validated against detailed velocity and pressure measurements. The present work aims at improving the prediction of the flow in a part of the water turbine before trying to include the full interaction between different parts of the water turbine.

2. THE COMPUTATIONAL CASES

It is very difficult to find publicly available water turbine runner geometries and detailed measurements of high quality. It is not common practice to make detailed pressure and velocity measurements during the development of new runners since it is the overall efficiency that is important at that stage. Detailed geometries, velocity measurements and pressure measurements of two kinds of water turbines that could be used for the present validation were however found: the GAMM Francis runner and the Hölleforsen Kaplan runner. The GAMM Francis runner was used as a test case in the 1989 *GAMM Workshop on 3D Computa-*

Table I. The GAMM operating conditions, where operating condition 1 is the best efficiency operating condition.

Operating condition	Volume flow rate coefficient $\varphi = Q/\pi\Omega R_{\text{ref}}^3$ [dimensionless]	Energy coefficient $\psi = 2E/\Omega^2 R_{\text{ref}}^2$ [dimensionless]	Efficiency $\eta = T\Omega/\rho QE$ [dimensionless]
1	0.286	1.07	0.920
2	0.220	0.66	0.850
3	0.330	1.40	0.910
4	0.220	1.07	0.885
5	0.330	1.07	0.905

tion of Incompressible Internal Flows [9] where the geometry and detailed best efficiency measurements were made available. In addition to the best efficiency measurements, four off-design operating condition measurements are used for the comparisons made in this work. The Hölleforsen Kaplan runner was used at the 1999 *Turbine 99* and 2001 *Turbine 99—II* workshops on draft tube flow [10, 11], where detailed measurements made after the runner were used as inlet boundary conditions for the draft tube computations. Unfortunately, in the case of the Hölleforsen runner, only the measurements are publicly available while the runner geometry is used in this work through a collaboration with the manufacturer, GE Energy (Sweden) AB.

The nomenclature used in this work is the same as that used at the workshops, which allows direct comparisons with the available measurements and facilitates understanding for those who are familiar with the nomenclatures of the workshops. Unfortunately, the nomenclatures are not the same in the two workshops, which must be kept in mind. The purpose is not to compare results between the Francis and Kaplan cases but rather to compare the computational results with the measurements. Thus the two nomenclatures should not pose any difficulties. The terms *absolute* and *relative* are used throughout this work to denote flow properties of the inertial and rotating co-ordinate systems, respectively.

The backgrounds of the cases are further described in the following sections.

2.1. The GAMM Francis runner

The GAMM Francis model was designed at IMHEF-EPFL, Lausanne. The model has 24 stay vanes, 24 guide vanes and 13 runner blades with a runner radius of $R_{\text{ref}} = 0.2$ m. The model was used as a test case in the 1989 *GAMM Workshop on 3D Computation of Incompressible Internal Flows* [9], where all the geometrical information, including stay vanes, guide vanes, runner and draft tube, and the best efficiency measurements were available. The runner is also available as a test case in the annual *ERCOFTAC Seminar and Workshop on Turbomachinery Flow Predictions* [12]. Of course, several off-design condition measurements have been made at IMHEF for internal use. Table I shows the operating conditions studied in this work. Here $Q[\text{m}^3/\text{s}]$ is the volume flow rate, $\Omega = 52.36\ \text{s}^{-1}$ is the runner angular rotation, $E[\text{J/kg}]$ is the specific hydraulic energy and $T[\text{Nm}]$ is the runner torque.

2.2. The Hölleforsen Kaplan runner

The Hölleforsen Kaplan model draft tube was thoroughly investigated at the 1999 *Turbine 99* and 2001 *Turbine 99—II* workshops on draft tube flow [10, 11]. The velocity distribution measured close to the runner blade suction side was used as an inlet boundary condition in the contributions at the workshop and the remainder of the measurements were used for validation of the draft tube computational results.

The model runner has a diameter of 0.5 m and has five runner blades and 24 guide vanes. The tip clearance (which is included in the computations) between the runner blades and the shroud is 0.4 mm. The computations are made at a head of $H = 4.5$ m, a runner speed of $N = 595$ rpm and a volume flow rate of $Q = 0.522\ \mathrm{m}^3/\mathrm{s}$. This operating condition is close to the best efficiency operating point.

3. NUMERICAL CONSIDERATIONS

The main features of the finite-volume CALC-PMB CFD code are its use of conformal block structured boundary fitted co-ordinates, a pressure correction scheme (SIMPLEC [13]), Cartesian velocity components as the principal unknowns, and a collocated grid arrangement together with Rhie and Chow interpolation [14]. Most hydraulic turbine computations found in the literature use the wall function approach to reduce the size of the computational domain. However, the wall function approach is based on local equilibrium assumptions in fully developed boundary layers, which is not found in water turbine runners. The present computations go one step further and use the low-Reynolds number $k-\omega$ turbulence model of Wilcox [15] to resolve the turbulent flow in clearances and boundary layers. Coriolis and centripetal effects are included in the momentum equations but not in the turbulence equations. This is common in turbomachinery computations for reasons of numerical stability and the small impact of such terms in these kinds of industrial applications. The discretization schemes used in this work are a second-order Van Leer scheme [16] for convection and a second-order central scheme for diffusion. The use of high-order discretization schemes in computations of water turbine runner flow is very important [17]. The computational blocks are solved in parallel with Dirichlet–Dirichlet coupling using parallel virtual machine (PVM) or message passing interface (MPI). The parallel efficiency is excellent, with super scalar speedup for load balanced applications [18]. The ICEM CFD/CAE grid generator is used for grid generation and Ensight and Matlab are used for post-processing.

The correct solution is assumed to be reached when the largest normalized residual of the momentum equations, the continuity equation and the turbulence equations is reduced to 10^{-3}. The momentum equation residuals are normalized by the sum of the mass flow through the turbine and the mass flow through the periodic surfaces multiplied by the largest value of the velocity component of each equation. The continuity equation residual is normalized by the sum of the mass flow through the turbine and the mass flow through the periodic surfaces. The turbulence equations residuals are normalized by the largest residual during the iterations.

The same computational method is used for both kinds of water turbines, where the steady, incompressible and periodic flow of a single runner blade is computed. Only the inlet boundary conditions and the geometries differ. The Francis runner computations obtain inlet boundary conditions from an extrapolation of the measurements and the Kaplan runner computation

obtains its inlet boundary condition from the circumferential average of a separate guide vane computation [17, 19]. All computations use axi-symmetric inlet boundary conditions for the velocity and turbulent quantities.

The computational grid for a single Hölleforsen guide vane passage consists of 285 177 control volumes. The computational grid for a single Hölleforsen runner blade passage consists of 722 157 control volumes, where 15 884 control volumes are in the tip clearance (19 control volumes in the runner blade tip to shroud direction) and 2 926 control volumes are in the hub clearance. The computational grid for a single GAMM runner blade passage consists of 560 736 control volumes.

3.1. Equations

The equations used for the computations are briefly described below.

The steady Reynolds time-averaged continuity and Navier–Stokes equations for incompressible flow in a rotating frame of reference read [20]

$$\frac{\partial \rho U_i}{\partial x_i} = 0$$

$$\frac{\partial \rho U_i U_j}{\partial x_j} = -\frac{\partial P}{\partial x_i} + \frac{\partial}{\partial x_j}\left((\mu + \mu_t)\frac{\partial U_i}{\partial x_j}\right) + \rho g_i - \rho \varepsilon_{ijk}\varepsilon_{klm}\Omega_j\Omega_l x_m - 2\rho\varepsilon_{ijk}\Omega_j U_k$$

where $-\varepsilon_{ijk}\varepsilon_{klm}\Omega_j\Omega_l x_m$ is the centripetal term and $-2\varepsilon_{ijk}\Omega_j U_k$ is the Coriolis term, owing to the rotating co-ordinate system. Because of the potential nature of the pressure, gravitational and centripetal terms [20], they are put together during the computations in what is often referred to as a *reduced* pressure gradient

$$-\frac{\partial P^*}{\partial x_i} = -\frac{\partial P}{\partial x_i} + \rho g_i - \rho \varepsilon_{ijk}\varepsilon_{klm}\Omega_j\Omega_l x_m$$

Thus, a relation for the *reduced* pressure is

$$P^* = P - \rho g_i x_i + \rho \varepsilon_{ijk}\varepsilon_{klm}\Omega_j\Omega_l x_m x_i$$

In post-processing, the variation of the gravity term is assumed to be negligible and the centripetal term is simply subtracted from the *reduced* pressure.

The low-Reynolds number $k-\omega$ turbulence model of Wilcox [15] for the turbulent kinetic energy, k, and the specific dissipation rate, ω, reads

$$\frac{\partial \rho U_j k}{\partial x_j} = \frac{\partial}{\partial x_j}\left[\left(\mu + \frac{\mu_t}{\sigma_k}\right)\frac{\partial k}{\partial x_j}\right] + P_k - \rho\beta^\star \omega k$$

$$\frac{\partial \rho U_j \omega}{\partial x_j} = \frac{\partial}{\partial x_j}\left[\left(\mu + \frac{\mu_t}{\sigma_\omega}\right)\frac{\partial \omega}{\partial x_j}\right] + \frac{\omega}{k}(c_{\omega 1}P_k - c_{\omega 2}\rho k\omega)$$

where the turbulent viscosity, μ_t, is defined as

$$\mu_t = \rho\frac{k}{\omega}$$

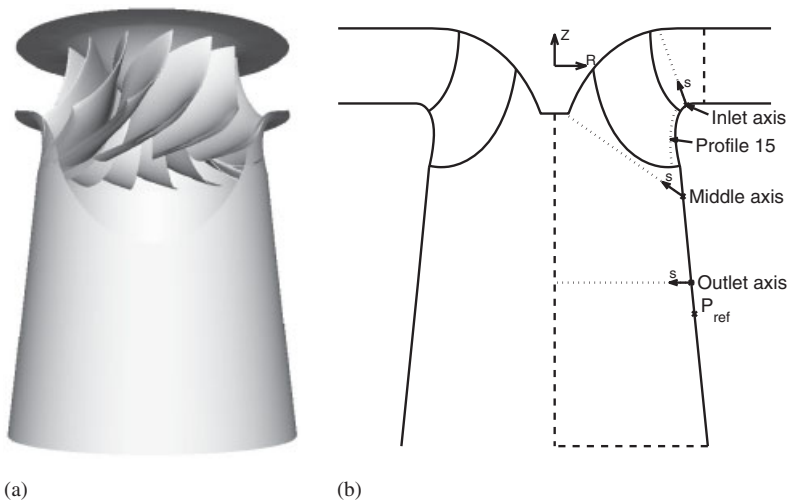

Figure 1. The GAMM Francis runner geometry, meridional contour (solid lines) and the domain that is computed (dashed lines). The domain has a radial inlet at the top and an axial outlet at the lower part of the figure. The dotted lines are sections in which the results are compared with measurements. Note that the inlet boundary conditions are extrapolated-from the measured inlet axis to the inlet of the computational domain. (a) The geometry; (b) Schematic meridional description.

The production term reads

$$P_k = \mu_t \left(\frac{\partial U_i}{\partial x_j} + \frac{\partial U_j}{\partial x_i} \right) \frac{\partial U_i}{\partial x_j}$$

and the closure coefficients are given by

$$\beta^\star = 0.09,\ c_{\omega 1} = \tfrac{5}{9},\ c_{\omega 2} = \tfrac{3}{40},\ \sigma_k = 2 \text{ and } \sigma_\omega = 2$$

A no-slip wall boundary condition is applied for the velocities and $k = 0$ at the walls. The specific dissipation at the first node normal to the wall (at $y^+ < 2.5$) is set to $\omega = 6\nu/(C_{\omega 2} n^2)$, where n denotes the normal distance to the wall. For the pressure, $\partial^2 P/\partial n^2 = 0$ at all boundaries. Dirichlet boundary conditions are applied at the inlet and Neumann boundary conditions are applied at the outlet for the velocity components and for the turbulent quantities.

3.2. *GAMM inlet boundary conditions*

The GAMM runner inlet velocity boundary conditions are obtained from an extrapolation of the inlet axis measurements (see Figure 1). This extrapolation assumes that there is no work done on the fluid in the extrapolation region and that the angular momentum and the mass flow are conserved. The axial velocity coefficient is set to zero. The reason for choosing this extrapolation technique is that it was used by Gros *et al.* [21] and its use here allows direct comparisons of the present computations with their computations.

The runner inlet boundary conditions for the turbulent quantities are difficult to prescribe. It is common in water turbine computations to assume a turbulent intensity and a turbulent

length scale and to apply constant turbulent properties at the inlet. The inlet turbulent kinetic energy in the present work is prescribed as

$$k_{\text{in}} = \frac{3}{2}\gamma^2 \overline{C_{\text{in}}}^2$$

where γ is the turbulent intensity and $\overline{C_{\text{in}}}^2$ is the inlet average absolute velocity squared. The turbulent length scale is used together with dimensional analysis to set the inlet boundary condition for ω as

$$\omega_{\text{in}} = \frac{k_{\text{in}}^{1/2}}{\beta^* l}$$

where $\beta^* = 0.09$ and l is the turbulent length scale. The computations made in this work assume a turbulent intensity of 5% and a turbulent length scale of $\frac{1}{3}$ of the inlet channel height. These numbers are somewhat arbitrary but it is not expected that their exact values are influential, since the source terms of the k and ω equations will be much larger than the history effects as soon as the flow reaches the runner. According to the ERCOFTAC description, the turbulent intensity was estimated to be 3%. It is, however, not specified how this value has been obtained.

3.3. Hölleforsen inlet boundary conditions

The Hölleforsen computation includes both the guide vanes and the runner (see Figure 2). The guide vane computational domain includes the runner duct, but the runner blades are not included in the computations. The inlet boundary for the runner computation is located between the guide vanes and the runner blades. The interaction between the rotating and stationary frames of references is numerically very complicated. A simple approach is used in this work where the computations are made in two steps. The flow at the guide vanes is first computed without the runner blades. The flow at the runner is then computed using the circumferentially averaged velocity and turbulence distributions from the guide vane computation as the inlet boundary condition. Upstream effects of the runner blades on the flow at the guide vanes are thus neglected. This is reasonable since LDV measurements reveal no upstream effects of the runner blades on the velocities at the guide vanes [17].

Since the flow in the spiral casing is not included in the computation, the flow at the inlet of the guide vane computation is assumed to be axi-symmetric and aligned with the guide vanes. A fully developed turbulent $\frac{1}{7}$ profile is used as the guide vane inlet boundary condition. The inlet turbulent kinetic energy is estimated by

$$k_{\text{in}} = C_{\mu}^{-0.5} l_m^2 \left(\frac{\partial U}{\partial y}\right)^2$$

where l_m is the Prandtl's mixing length and is given by

$$l_m = \min(\kappa y, \lambda\delta)$$

where $\kappa = 0.41$ is the von Karman constant, $\lambda = 0.09$, y is the distance from the nearest wall and δ is the inlet height. This relation stems from the assumption of turbulence-energy

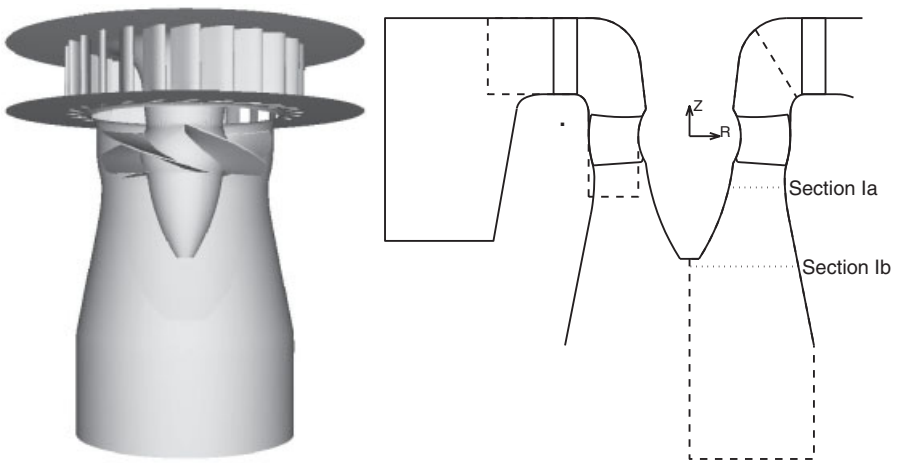

(a) (b)

Figure 2. The Hölleforsen Kaplan runner geometry, meridional contour (solid lines) and the domains that are computed (dashed lines). The left domain is the guide vane domain, with a radial inlet in the spiral casing region and an axial outlet in the runner region. The right domain is the runner domain, with a tilted inlet between the guide vanes and the runner blades and an axial outlet at the lower part of the figure. The dotted lines are sections in which the results are compared with measurements. (a) The geometry; (b) Schematic meridional description.

equilibrium, i.e. the production of turbulent kinetic energy is balanced by its dissipation. The inlet specific dissipation is set according to

$$\omega_{\text{in}} = \frac{\rho k_{\text{in}}}{10\mu}$$

4. VALIDATION AGAINST MEASUREMENTS

The following sections compare the computed results with the available measurements.

4.1. GAMM comparisons

This section compares the GAMM runner computational results with measurements of the best efficiency operating condition [9] and four off-design operating conditions (see Table I). The runner measurement sections (inlet axis, middle axis and outlet axis) are shown in Figure 1, where the abscissas, s, are aligned with the measurement axes and normalized by $R_{\text{ref}} = 0.2$ m. The runner blade surface static pressure of the computations is compared with the measurements at profile 15 (see Figure 1). The velocities and the static pressure are normalized with $\sqrt{2E}$ and ρE, respectively, where E is the specific energy of each operating condition.

The normalized velocity coefficients, C_v, are the tangential (C_u, positive in the runner rotation direction), the axial (C_z, positive along the Z-axis), the radial (C_r, positive in the R-direction) and the meridional ($C_{\text{m}} = \sqrt{C_r^2 + C_z^2}$, always positive). The absolute and relative

flow angles are given in degrees and are defined as

$$\alpha = \arctan\left(\frac{C_{\mathrm{m}}}{C_u}\right) \tag{1}$$

$$\beta = \arctan\left(\frac{C_{\mathrm{m}}}{\Omega R/\sqrt{2E} - C_u}\right) \tag{2}$$

The static pressure coefficient is defined as

$$C_p = \frac{P - P_{\mathrm{ref}}}{\rho E}$$

where the reference static pressure, P_{ref}, was measured at the reference point on the shroud (see Figure 1).

The accuracy of the test instrumentation was claimed to be far better than the IEC model turbine acceptance test code requirements [22]. The measurement method is, however, inadequate in regions of high unsteadiness and recirculation, where the measurements are not reliable.

4.1.1. Velocity profiles. Figures 3–5 compare the circumferentially averaged computed and measured velocity coefficient distributions and flow angles at the measurement axes. At the inlet axis, one evaluation point of the circumferentially averaged results is located in the hub boundary layer, which is why there is a sudden change in velocity coefficients and flow angles to the right in the graphs. Note that the hub is rotating, which explains why the tangential velocity coefficient is non-zero at the hub.

It should be noted that the computations satisfy mass conservation. Thus, the disagreement in the level between the computed and measured meridional velocity distributions must originate in non-periodicity of the experimental flow, in a normalization error or in measurement errors.

The computational results mainly differ from the measurements close to the axis of rotation after the runner. This is particularly true at operating conditions 2 and 4, where the mass flow was low and a strong unsteady vortex rope formed in the experimental set-up. Neither the computational assumptions of steady periodic flow nor the experimental method is sufficient in this region of high instabilities and recirculation. Thus better measurement techniques and numerical methods are both needed to study the flow in this region.

4.1.2. Outlet axis static pressure distribution. Figure 6 shows the good agreement achieved between the measured and computed static pressure coefficients at the outlet axis of operating condition 1.

4.1.3. Runner blade static pressure distribution. Figure 7 compares the computed and measured static pressure distributions along profile 15 (see Figure 1). The abscissa, s, is the distance from the leading edge along the surface of the blade profile normalized by R_{ref}. The computations yield the same distributions as the measurements.

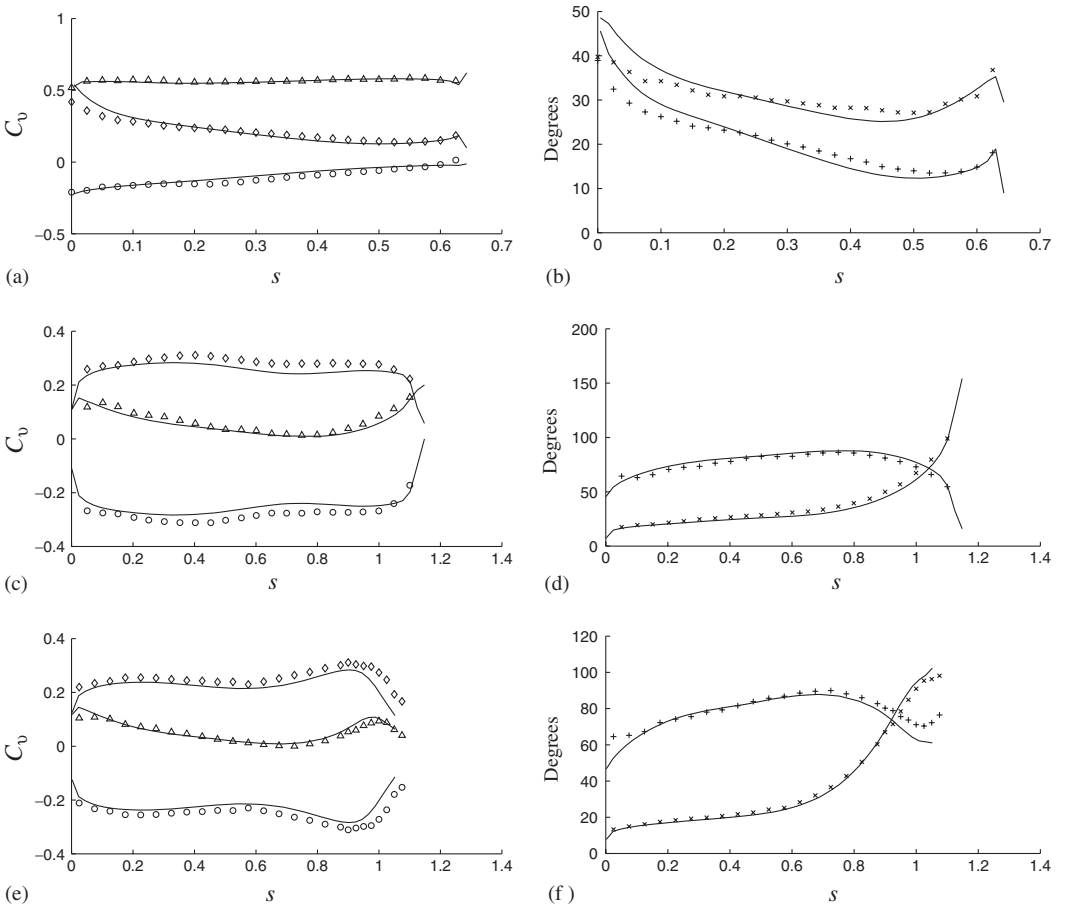

Figure 3. GAMM operating condition 1 flow survey. Solid lines: circumferentially averaged computational results. Measurement markers: △: Tangential, ○: Axial, ◇: Meridional, +: Absolute (α), ×: Relative (β). (a) Inlet axis absolute velocity coefficients; (b) Inlet axis flow angles; (c) Middle axis absolute velocity coefficients; (d) Middle axis flow angles; (e) Outlet axis absolute velocity coefficients; (f) Outlet axis flow angles.

4.1.4. Comparisons with previous computations. Computations similar to those presented in the present work have been made by Gros *et al.* [21]. The computations by Gros *et al.* were made on a coarse mesh with less than 100 000 nodes for a single runner blade passage, which should be compared with the 560 736 control volumes in the present work. The standard $k-\varepsilon$ turbulence model with wall functions was used by Gros *et al.* in order for the computing time to be reasonable for industrial use. Gros *et al.* used the TASCflow and N3S commercial CFD codes and compared the computational results with the same measurements as in this work. A coupled TASCflow computation of the best efficiency operating condition including stay vanes, guide vanes and runner was also made.

Figure 8 shows a comparison between some of the results from the present work and the corresponding TASCflow results of Gros *et al.* The computational results of the present work

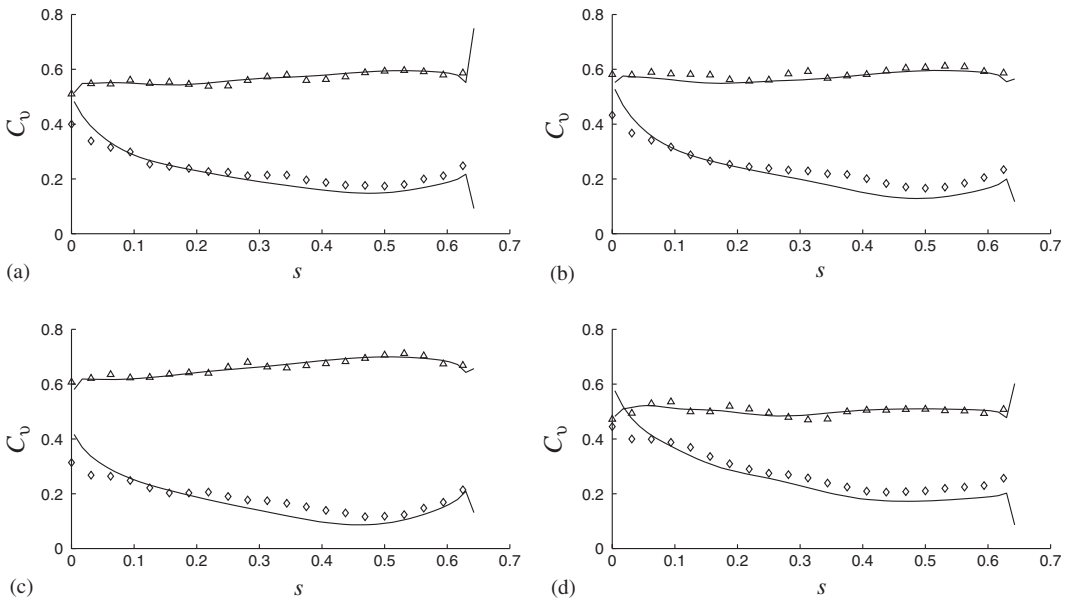

Figure 4. GAMM operating condition 2–5 flow surveys. Inlet absolute velocity coefficients. Solid lines: circumferentially averaged computational results. Measurement markers: △: Tangential, ◇: Meridional. (a) Operating condition 2; (b) Operating condition 3; (c) Operating condition 4; (d) Operating condition 5.

are slightly better than the TASCflow results and both codes qualitatively capture the same flow features. The coupled TASCflow computation at operating condition 1 does not improve the results by Gros *et al.* The N3S computations by Gros *et al.* were less reliable [21] and are therefore not included in this comparison. The CALC-PMB and TASCflow CFD codes are very similar and both use structured grids, while the N3S CFD code uses unstructured grids. The structured grid approach thus seems to be the best approach.

4.2. Hölleforsen comparisons

The following sections compare the Hölleforsen Kaplan runner computational results with the detailed experimental results that were available at the *Turbine 99* workshop [10, 11].

4.2.1. Velocity profiles. The computational results are compared with the *Turbine 99* LDV measurements at Sections Ia and Ib (see Figure 2). The velocity coefficients, C_v, are the velocities normalized by Q/A_i, where Q is the volume flow rate and A_i is the area of each section ($Q = 0.522\ \mathrm{m}^3/\mathrm{s}$, $A_i = 0.15\ \mathrm{m}^2$ for Section Ia and $A_i = 0.23\ \mathrm{m}^2$ for Section Ib). The absolute tangential velocity is defined as positive when the flow is co-rotating with the runner, and the axial velocity is defined as positive in the main flow direction which is downward at Sections Ia and Ib. The radial velocity is defined as positive when the flow is outward from the axis of rotation.

Figure 9(a) compares the circumferentially averaged computed and measured velocity distributions at Section Ia. The computed velocity distributions are very similar to the measurements

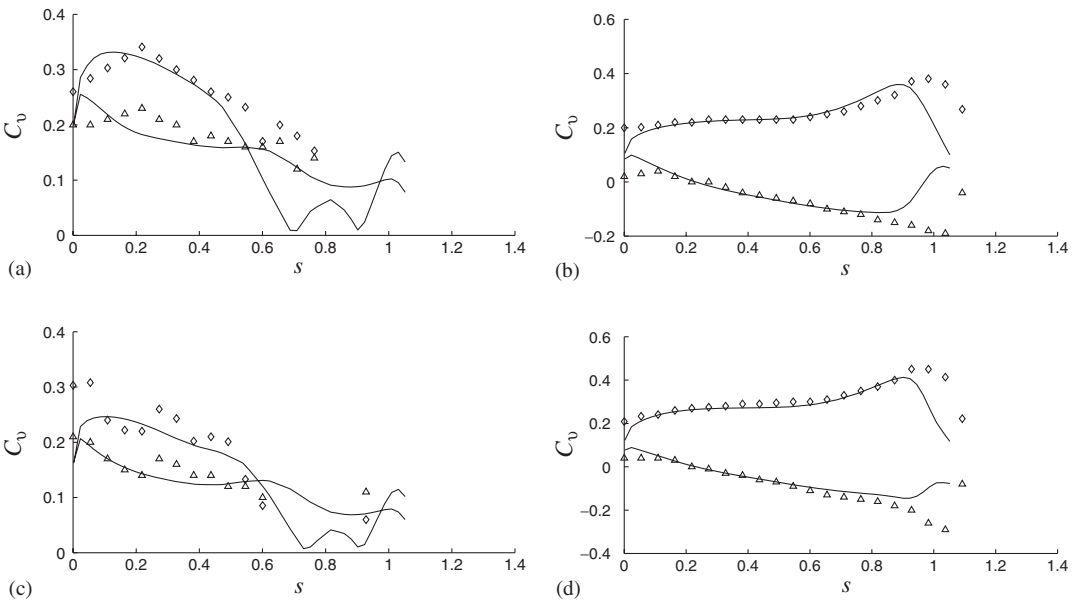

Figure 5. GAMM operating condition 2–5 flow surveys. Outlet absolute velocity coefficients. Solid lines: circumferentially averaged computational results. Measurement markers: △: Tangential, ◇: Meridional. (a) Operating condition 2; (b) Operating condition 3; (c) Operating condition 4; (d) Operating condition 5.

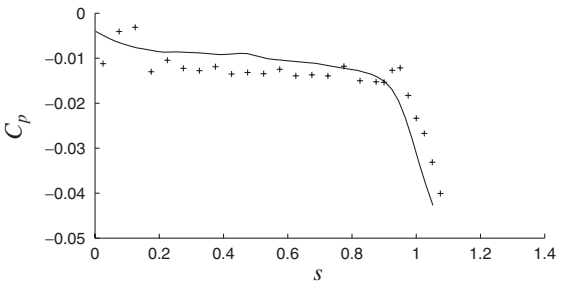

Figure 6. GAMM operating condition 1. Outlet axis static pressure coefficient distribution. Solid lines: circumferentially averaged computational results, +: measurements.

in the outer region (large radius), while they differ slightly from the measurements in the inner region. The main difference is the lack of a peak in the predicted axial velocity close to the shroud. Andersson [23] argued that this peak originated in the leakage between the runner hub and the runner blades. This leakage is included in the computations but they do not capture this effect. Both supplementary measurements and computations suggest that the effect more likely originates from boundary layer effects that are already present in the spiral casing [17], which is not included in the computations. It should be noted that the LDV technique used in the experiments has problems making measurements close to surfaces, and the measurement points closest to the hub are thus unreliable [19].

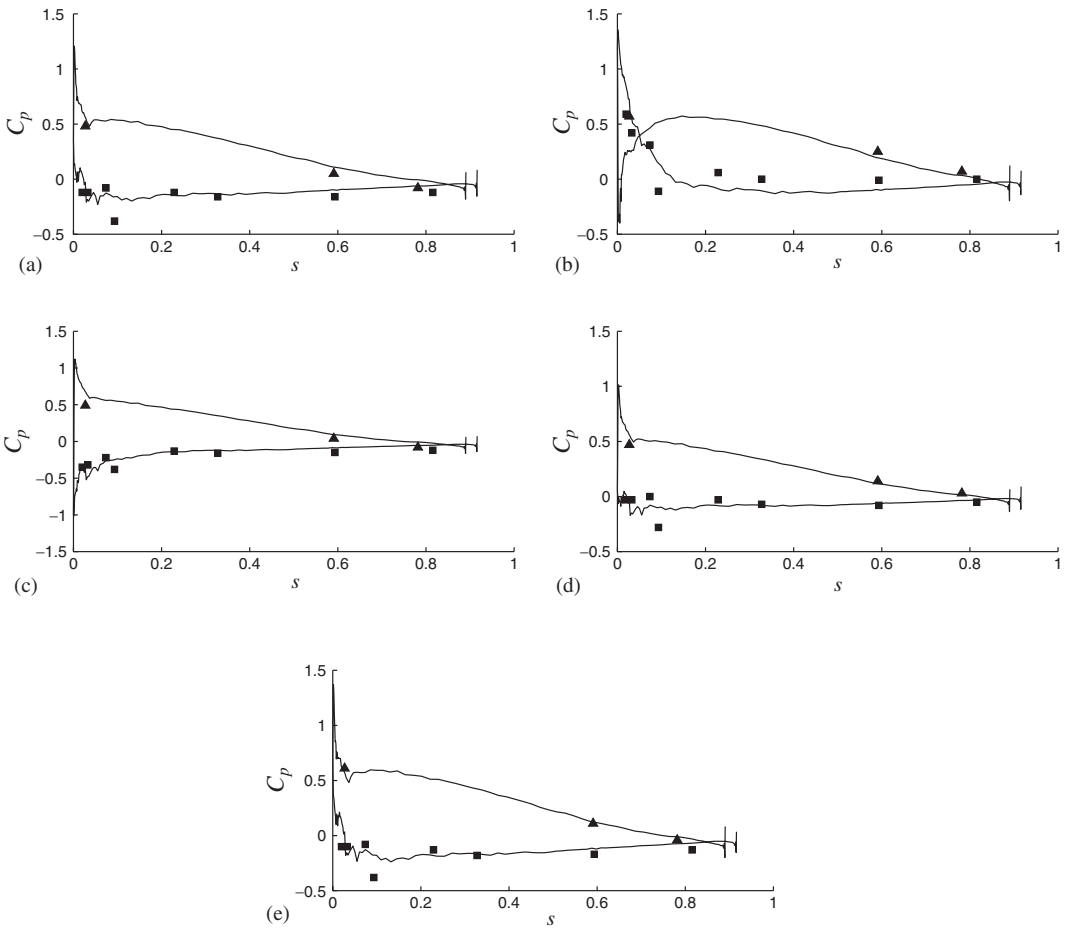

Figure 7. GAMM runner. Surface static pressure coefficient, profile 15. Solid lines: computational results. Measurement markers: ▲: Pressure side, ■: Suction side. (a) Operating condition 1; (b) Operating condition 2; (c) Operating condition 3; (d) Operating condition 4; (e) Operating condition 5.

Figure 9(b) compares the circumferentially averaged computed and measured velocity distributions at Section Ib. The computed flow captures some of the main features of the experimental flow. The flow in the axial diffusor after the runner is very difficult to capture, particularly close to the hub [17]. The periodic and steady assumptions lack the same validity in this region, where the experimental flow has a vortex rope formation with inherent instability and recirculation. Experimental visualizations indicated a small recirculation region close to the rotational axis at section Ib, and both mean and RMS values of the velocity measurements and the visualizations indicated a vortex rope that extended to about $r^* = r/R = 0.25$ [23]. The model draft tube bend also causes streamline curvature below the runner.

It should be noted that the velocity measurements at Sections Ia and Ib presented in Figure 9 were made at a single tangential angle, which does not take into account the tangential variation. Measurements indicate a non-negligible tangential variation of 2% and 15% for the axial and tangential components, respectively, at Section Ia [23]. Furthermore, the operating

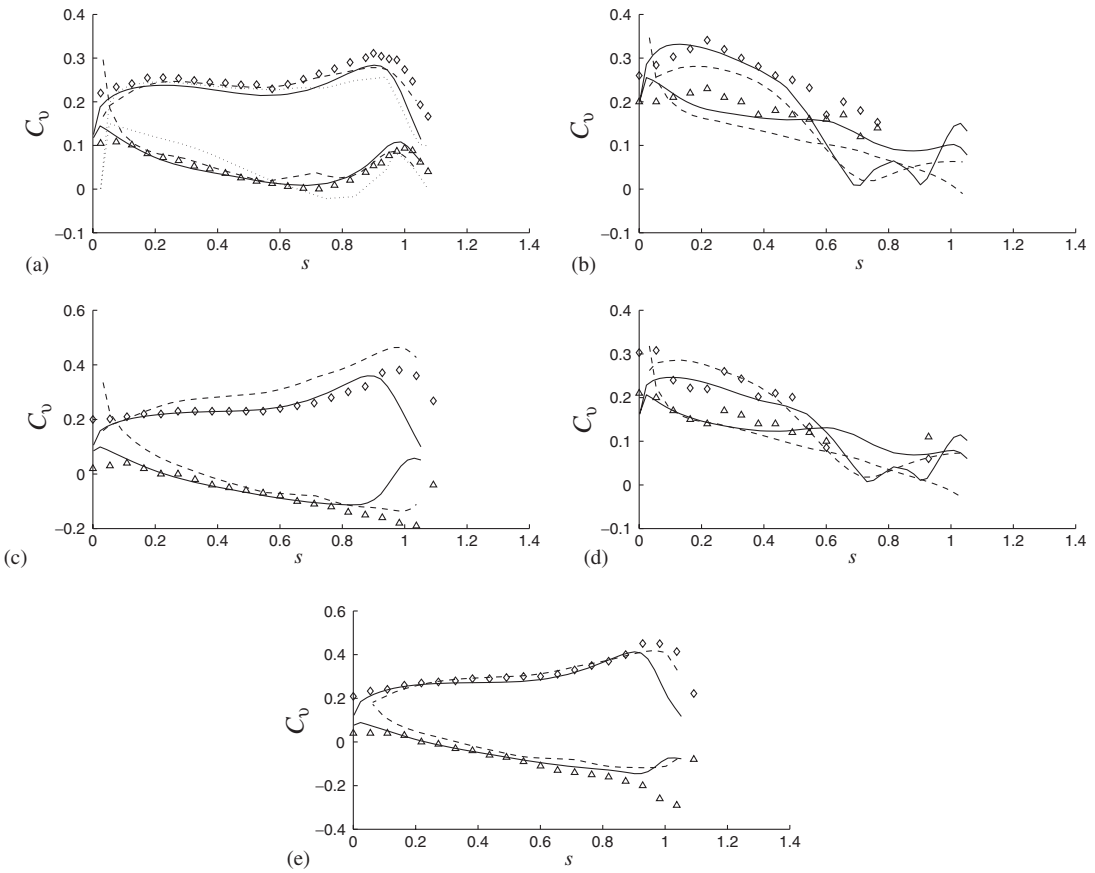

Figure 8. GAMM runner outlet absolute velocity coefficients. Comparison between the present computations and the computations by Gros *et al.*. Solid lines: present computations, dashed lines: Gros *et al.*, dotted line: Gros *et al.* coupled computation. Measurement markers: △: Tangential, ◇: Meridional. (a) Operating condition 1; (b) Operating condition 2; (c) Operating condition 3; (d) Operating condition 4; (e) Operating condition 5.

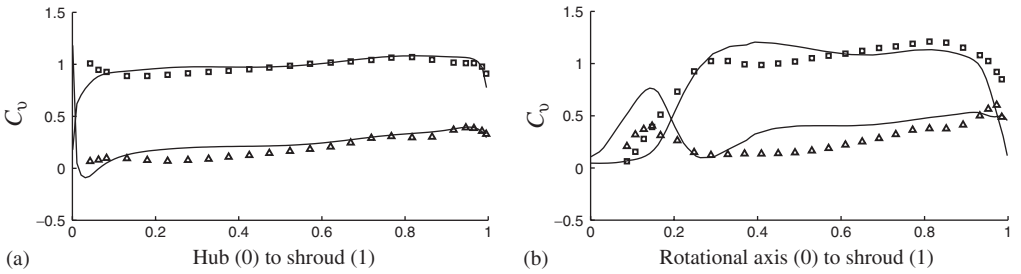

Figure 9. Hölleforsen velocity coefficient distributions. Solid lines: computational results. Measurement markers: △: tangential; □: axial. (a) Section Ia; (b) Section Ib.

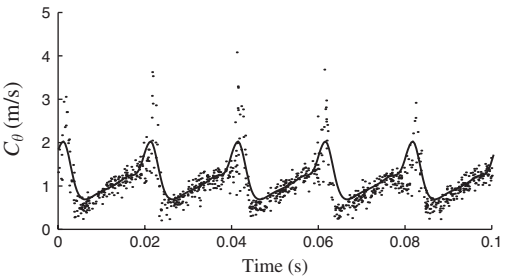

Figure 10. Hölleforsen comparison between computed and measured periodic behaviour of the tangential velocity component at $r^* = r/R = 0.92$ at section Ia. Dots: individual measurement samples; solid line: computational results. The computational results have been phase shifted to match the measurements because it was not possible to obtain the exact runner angles of the measurements. One runner revolution (five blades passages) takes approximately 0.1 s.

condition altered slightly during the measurements because of hardware problems. The velocity measurements were more sensitive to this than the overall efficiency and pressure recovery were [11].

4.2.2. Runner blade wakes. The computation resolves a periodic behaviour of the wake at Section Ia, as shown experimentally by Andersson [23]. Figure 10 compares the computed and measured periodic behaviour of the tangential velocity component at $r^* = r/R = 0.92$ at Section Ia.

There are distinct peaks in the tangential velocity component in the wake regions. The magnitude of the peak seems to be much greater in the measurements. However, phase averaging the measurements yields results similar to those of the computation.

4.2.3. Pressure recovery. At the *Turbine 99* workshop, Andersson [23] presented the pressure recovery of the draft tube from Section Ia to the outlet of the draft tube. Figure 11 compares the computed pressure recovery with the measured pressure recovery in the axial diffusor. The pressure recovery

$$C_{\mathrm{Pr}} = \frac{P_{\mathrm{wall}} - P_{\mathrm{wall,Ia}}}{P_{\mathrm{dyn,Ia}}}$$

is normalized with the dynamic pressure at Section Ia: $P_{\mathrm{dyn,Ia}} = \rho Q^2/(2A_{\mathrm{Ia}}^2) = 6.48$ kPa ($Q = 0.522\ \mathrm{m}^3/\mathrm{s}$, $A_{\mathrm{Ia}} = 0.145\ \mathrm{m}^2$, $\rho = 1000\ \mathrm{kg/m}^3$). P_{wall} is the average of the measured pressure at two sides of the draft tube cone. For the computational results, P_{wall} is the circumferential average of the pressure at the draft tube cone wall, since the computational domain is rotating. $P_{\mathrm{wall,Ia}}$ is the corresponding value at Section Ia.

5. CONCLUSION

The present work validates CFD against detailed velocity and pressure measurements in water turbine runner flow. Two kinds of water turbine runners and several operating conditions are

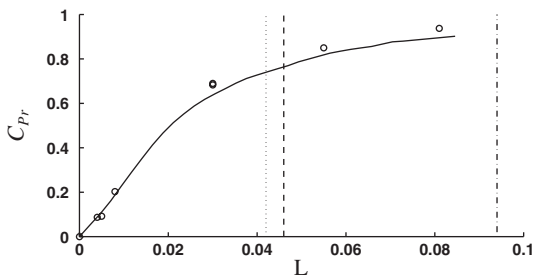

Figure 11. Hölleforsen comparison between computed and measured pressure recovery between Section Ia and the end of the draft tube cone. ○: measured pressure coefficient; solid curve: computed pressure coefficient. The vertical lines show some important locations: dotted line: end of runner cone; dashed–dotted line: Section Ib; dashed line: end of draft tube cone. The abscissa, L, is 0 at Section Ia and 1 at the end of the draft tube.

studied. The computational results qualitatively capture the main features of the experimental flow. There are, however, general problems in predicting the flow accurately at small radius. The reason to this can be related to discretization, turbulence modelling, inadequate boundary conditions or omission of interaction with the rest of the system. The periodic and steady assumptions used in the present work are inadequate in the region close to the axis of rotation after the runner, where the experimental flows have a vortex rope formation with inherent instability and recirculation, and the model draft tube bend causes streamline curvature. The measurement techniques also need improvements to accurately study the flow in this region.

Some of the present computational results are compared with previous computational results by Gros *et al.* [21]. The difference between the computations is the use of a low-Reynolds number turbulence model in the present work instead of the wall function approach used by Gros *et al.* The integration up to the wall and a fine resolution of the viscous sublayer cannot be avoided if transition phenomena and accurate wall friction are to be solved. The CALC-PMB CFD code used in the present work and the TASCflow CFD code used by Gros *et al.* are both finite-volume CFD codes and both use multiblock structured grids. Both codes qualitatively capture the same flow features but the present results are slightly more accurate in most of the comparisons. A coupled computation including stay vanes, guide vanes and runner did not improve the results by Gros *et al.*

One of the two water turbine runners studied in the present work is publicly available and one is not. In order to advance the state of the art in CFD in water turbines there need to be more publically available test cases with detailed measurements. A united effort is needed, involving several researchers from both the experimental, the theoretical and the computational research communities.

ACKNOWLEDGEMENTS

This work is financed and supported by ELFORSK (Swedish Electrical Utilities Research and Development Company), the Swedish National Energy Administration and GE Energy (Sweden) AB.

Vattenfall Utveckling AB and its staff, particularly Urban Andersson and Rolf Karlsson, are gratefully acknowledged for their contributions.

GE Energy (Sweden) AB and its staff, particularly Bengt Nauclér, are gratefully acknowledged for information on geometry and for their support.

Professor F. Avellan and the staff at IMHEF-EPFL in Lausanne are gratefully acknowledged for making the off-design measurements available.

Computational resources at UNICC, Chalmers, are gratefully acknowledged.

REFERENCES

1. Lakshminarayana B. *Fluid Dynamics and Heat Transfer of Turbomachinery*. Wiley Inc.: New York, 1996.
2. Muntean S. Numerical methods for the analysis of the three-dimensional flow in Francis turbine runners. *Thesis for the degree of Doctor of Philosophy*, Mechanical Engineering Faculty, University of Timisoara, 2002.
3. Maji PK, Biswas G. Analysis of flow in the plate-spiral of a reaction turbine using a streamline upwind Petrov–Galerkin method. *International Journal for Numerical Methods in Fluids* 2000; **34**:113–144.
4. Vu TC, Shyy W. Viscous flow analysis as a design tool for hydraulic turbine components. *Journal of Fluids Engineering* 1990; **112**:5–11.
5. Avellan F, Ciocan G, Kvicinsky S (eds). Hydraulic Machinery and Systems. *Proceedings of the XXIst IAHR Symposium*. EPFL Laboratoire de machines hydraulic, 2002.
6. Cobut D *et al.* A numerical study of the flow in a Francis turbine runner at off-design operating conditions. *Conference on Modeling, Testing & Monitoring for Hydro Powerplants—II, IMHEF Report T*-96-14, 1996.
7. Ruprecht A *et al.* Massively parallel computation of the flow in hydro turbines. *Proceedings of the XXIst IAHR Symposium*, vol. 1, 2002; 199–206.
8. Hanjalić K. Second moment turbulence closures for CFD: needs and prospects. *International Journal of Computational Fluid Dynamics* 1999; **12**:67–97.
9. Sottas G, Ryhming IL (eds). 3D Computations of Incompressible Internal Flows. *Proceedings of the GAMM Workshop*, Lausanne—Notes on Numerical Fluid Mechanics. Vieweg: Braunschweig, 1993; 55–62.
10. Andersson U. An experimental study of the flow in a sharp-heel draft tube. *Thesis for the degree of Licentiate of Engineering*, Department of Mechanical Engineering, Division of Fluid Mechanics, Luleå University of Technology, 2000; ISSN: 1402-1757.
11. Andersson U, Karlsson R. Quality aspects of the Turbine 99 draft tube experiment. In *Proceedings of Turbine 99—Workshop on Draft Tube Flow*, 2000; ISSN: 1402-1536.
12. Parkinson E. Turbomachinery Workshop ERCOFTAC II, test case 8: Francis turbine. *IMHEF Report T*-91-3, 1995.
13. Van Doormaal JP, Raithby GD. Enhancements of the SIMPLE method for predicting incompressible fluid flows. *Numerical Heat Transfer* 1984; **7**:147–163.
14. Rhie CM, Chow WL. Numerical study of the turbulent flow past an airfoil with trailing edge separation. *AIAA Journal* 1983; **21**:1525–1532.
15. Wilcox DC. Reassessment of the scale-determining equation for advanced turbulence models. *AIAA Journal* 1988; **26**(11):1299–1310.
16. van Leer B. Towards the ultimate conservative difference scheme. Monotonicity and conservation combined in a second order scheme. *Journal of Computational Physics* 1974; **14**:361–370.
17. Nilsson H. Numerical investigations of turbulent flow in water turbines. *Thesis for the degree of Doctor of Philosophy*, Department of Thermo and Fluid Dynamics, Chalmers University of Technology, Gothenburg, 2002.
18. Nilsson H, Dahlström S, Davidson L. Parallel multiblock CFD computations applied to industrial cases. In *Parallel Computational Fluid Dynamics—Trends and Applications*, Jenssen CB *et al.* (eds). Elsevier: Amsterdam, 2001; 525–532.
19. Nilsson H, Davidson L. A numerical investigation of the flow in the wicket gate and runner of the Hölleforsen (Turbine 99) Kaplan turbine model. In *Proceedings of the Turbine 99 II Workshop on Draft Tube Flow*, 2001.
20. Kundu PK. *Fluid Mechanics.* Academic Press: San Diego, CA, 1990.
21. Gros L, Kueny JL, Avellan F, Bellet L. Numerical flow analysis of the GAMM turbine at nominal and off-design operating conditions. In *Proceedings of the XIX IAHR Symposium*, Hydraulic Machinery and Cavitation, 1998; 121–128.
22. Avellan F, Dupont P, Farhad M, Gindroz B, Henry P, Hussein M, Parkinson E, Santal O. Experimental flow study of the GAMM turbine model. In *3D Computations of Incompressible Internal Flows—Proceedings of the GAMM Workshop at EPFL*, Sottas G, Ryhming IL (eds), September 1989, Lausanne—Notes on Numerical Fluid Mechanics. Vieweg: Braunschweig, 1993; 33–53.
23. Andersson U. Turbine 99—experiments on draft tube flow (test case T). In *Proceedings of Turbine 99—Workshop on Draft Tube Flow*, 2000; ISSN: 1402-1536.

